



Effects of 1,8-Diiodooctane on Domain Nanostructure and Charge Separation Dynamics in PC71BM-Based Bulk Heterojunction Solar Cells

Journal:	<i>Journal of Materials Chemistry A</i>
Manuscript ID	TA-ART-07-2018-006865.R1
Article Type:	Paper
Date Submitted by the Author:	12-Oct-2018
Complete List of Authors:	Lou, Sylvia; Northwestern University, Department of Chemistry Zhou, Nanjia ; Northwestern University Guo, Xugang; South University of Science and Technology of China, Materials Science and Engineering Chang, Robert; Northwestern University, Department of Materials Science and Engineering Marks, Tobin; Northwestern University, Department of Chemistry Chen, Lin; Northwestern University, Chemistry; Argonne National Laboratory, Chemical Sciences and Engineering

Effects of 1,8-Diiodooctane on Domain Nanostructure and Charge Separation Dynamics in PC₇₁BM-Based Bulk Heterojunction Solar Cells

Sylvia J. Lou,¹ Nanjia Zhou,² Xugang Guo,^{1,3} Robert P. H. Chang,^{2*} Tobin J. Marks,^{1,2*} Lin X. Chen^{1,4*}

Affiliations

¹ Department of Chemistry and the Argonne-Northwestern Solar Energy Research Center, Northwestern University, 2145 Sheridan Road, Evanston, Illinois 60208, United States

² Department of Materials Science and Engineering and the Argonne-Northwestern Solar Energy Research Center, Northwestern University, Evanston, Illinois 60208, United States

³ Department of Materials Science and Engineering, South University of Science and Technology of China, No. 1088, Xueyuan Blvd, Shenzhen, Guangdong, 518055, China

⁴ Chemical Sciences and Engineering Division, Argonne National Laboratory, Darien, Illinois 60439, United States

*Email - t-marks@northwestern.edu

Abstract

Processing additives are commonly used to optimize phase separation morphology and power conversion efficiency (PCE) in the bulk heterojunction (BHJ) organic photovoltaics (OPVs), however their exact effects are not well understood. The bulk-heterojunction OPV system containing the model bithiophene imide-benzodithiophene copolymer (PBTIBDT): phenyl-C₇₁-butyric-acid-methyl ester (PC₇₁BM) exhibits a maximum PCE of 5.4% with addition of 3.0 vol% 1,8-diiodooctane (DIO). Here the effects of increasing DIO concentrations (0 → 5 vol%) on the PBTIBDT:PC₇₁BM solutions and resulting thin films are studied by X-ray scattering methodologies and transient optical absorption spectroscopy with 0.1 ps time resolution. As the DIO concentration increases, the radius of gyration of the PC₇₁BM aggregates falls from 17 Å to 9 Å in solution, and TEM indicates the formation of

increasing PC₇₁BM charge percolation pathways in the thin BHJ films. Increased PBTIBDT + PC₇₁BM intermixing not only affects BHJ film charge transport, but also enhances the initial exciton splitting yield in the PBTIBDT cation population. In contrast, the hole carrier population (as represented by the polymer cation) detected several nanoseconds after the photoexcitation is greatest with 3.0 vol% DIO, agreeing well with the corresponding BHJ composition for maximum OPV short circuit current density (J_{sc}) and fill factor (FF). The increase in initial polymer cation yield with DIO concentration is attributed to enhanced donor-acceptor interfacial area while the increase in long-lived cation population is attributed to formation of a bicontinuous donor polymer - PC₇₁BM acceptor network that promotes large spatial separation of free charges in the device active layer. These results demonstrate the importance of OPV function on the correct balance, as tuned by processing additives, between a high initial donor cation formation yield and high carrier transport efficiency with minimized charge recombination rate.

Introduction

Recent advances in power conversion efficiency (PCE) of organic photovoltaic (OPV) devices demonstrate their potential in providing electricity via alternative energy sources.¹⁻⁵ Until very recently, most of these single-junction OPVs were bulk heterojunction (BHJ) devices in which the charge-generating active layer consists of a mixture of a p-type electron donor polymer⁶⁻⁹ and a fullerene-based electron acceptor such as phenyl-C₇₁-butyric-acid-methyl ester (PC₇₁BM). Excitons formed upon light illumination in the polymer domain subsequently dissociate at the polymer-PC₇₁BM interfaces into holes and electrons, when the LUMO-LUMO energetic offset between the donor polymer and the acceptor PC₇₁BM is sufficient to overcome the exciton binding energy. The holes and electrons generated via exciton splitting travel through their respective contiguous polymer and PC₇₁BM domains to the appropriate charge-collecting electrodes. Despite the recent rise in power

conversion efficiencies (PCEs) to over 14% (ref), the design of consistently high-performing BHJ polymer solar cells presents a challenge, reflecting incomplete understanding of the inherent energetic and morphological complexity of these systems.¹⁰⁻²²

Energetic models of ideal solar cell polymers have been articulated^{10, 23} and provide impetus for the design of many current-generation donor polymers.^{9, 24} However, it is well known that even polymers with “perfect” energetic characteristics may not exhibit correspondingly high PCEs due to limitations in either the short circuit current (J_{sc}) or fill factor (FF), as well as local structural irregularities.²⁵⁻³¹ In contrast, the common key criteria in molecular design, the LUMO-LUMO energy offset between the donor and acceptor materials and the open circuit voltage (V_{oc}) have poor correlations with device PCE.³¹ This result and the lack of device performance predictability suggest that the origin of poor device performance is most likely “non-ideal morphology,” where, in extreme cases, either the polymer and the fullerene are fully segregated with relatively small or energetically unfavorable interfacial boundaries,^{2, 27, 29} thereby compromising efficient charge generation, or the two are completely intermixed resulting in a loss of domain connectivity, creating high densities of charge-trapping islands.²⁵ Many fabrication techniques have been utilized to improve the morphology of BHJ systems including thermal annealing,^{15, 32-40} polymer:fullerene ratio optimization,⁴¹⁻⁴⁶ and solvent additives.^{37, 47-53} In particular, solvent additives have provided significant control over film morphology since they facilitate independent formation of polymer and fullerene domains based on their different solubilities.⁵⁴⁻⁵⁷ Typically, appropriate solvent additives have high boiling points compared to commonly used film casting solvents (e.g., chlorobenzene, chloroform, toluene, etc.) which extends the time for the polymer and fullerene to organize into ordered domains.⁵⁸⁻⁶³

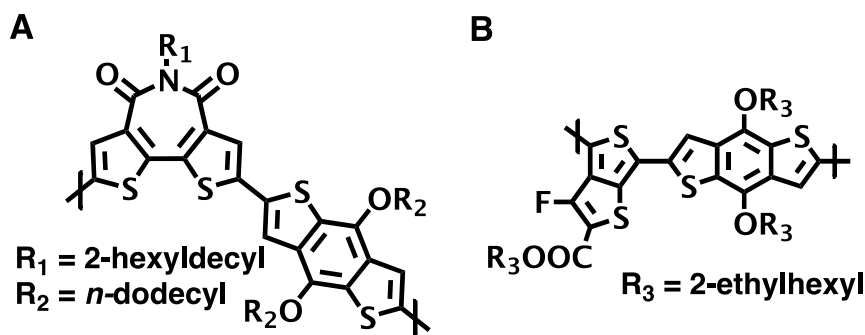
Previous work has amply demonstrated that the addition of solvent additives modifies the resulting BHJ film morphology^{58, 60, 64-72} and energetics,^{73, 74} although the exact effects vary with the solvent additive and polymer system. Broadly speaking, solvent additives can play either of two roles

to balance film morphology. In some cases, they improve polymer + PC₇₁BM domain formation and phase segregation and often concurrently, solubilize the polymer alkyl side chain substituents, promoting the formation of more crystalline and pure polymer domains.^{58, 62, 63, 69, 75, 76} For systems in which the polymer and PC₇₁BM are very miscible, OPVs without solvent additives exhibit high levels of charge recombination due to the formation of PC₇₁BM “islands” that prevent long-range charge transport after exciton splitting and hence result in charge trap creation, leading to geminate charge recombination.^{60, 69, 75} In other cases, solvent additives break up large segregated domains and/or create more mixed phase domains. For example, when 3 vol% DIO is added to the PTB7:PC₇₁BM system, the domains decrease in size leading to significantly increased J_{sc} and FF , and a corresponding PCE increase by 150%.^{64, 65, 77} We have previously attributed the enhanced morphology in the PTB7:PC₇₁BM system with DIO to the selective dissolution of PC₇₁BM aggregates in DIO, favoring the creation of a more interpenetrated PTB7-PC₇₁BM network via slow crystallization.^{62, 78}

In general, while BHJ morphology optimization must simultaneously enable effective exciton splitting and rapid charge transport in OPV device active layers, an optimal morphology for a particular BHJ system is often challenging to predict and control. While the active layer film morphology can range from a uniform distribution of donor and acceptor (one-phase morphology) at one extreme to large crystalline donor and/or acceptor domains (two-phase morphology) at the other, most polymer solar cells encompass a three-phase morphology consisting of pure donor domains, pure acceptor domains, and intermixed donor-acceptor regions on multiple length scales.⁷⁹⁻⁸² Note that while charge transport is facilitated by the pure polymer and PCBM domains, mixed domains provide sufficient donor-acceptor interfacial area to promote the essential step of charge separation.

In BHJ systems some mixing of the donor polymer and PC₇₁BM is inevitable, however the nature of the mixing can vary widely from regularly intercalated PC₇₁BM in crystalline polymer networks

(e.g., pBTTT)^{81, 83-87} to fully blended amorphous polymers with PC₇₁BM.^{65, 88-93} In the former, it is found that increased PC₇₁BM intercalation into the pBTTT crystalline network affords increased charge separated populations and J_{sc} , but also increased geminate charge recombination⁹⁴ and decreased FF due to the lack of continuous electron transporting PC₇₁BM networks.⁸⁴ Similarly, in OPVs with semi-crystalline or amorphous donor polymers, smaller pure PC₇₁BM and polymer



Scheme 1. Chemical structures of the electron donor polymers A) PBTIBDT and B) PTB7.

domains and hence, increased polymer–PC₇₁BM interfacial areas, afford increased charge-separated state populations,⁹⁵⁻⁹⁷ and/or decreased charge transfer state populations.^{10, 98, 99} However, large donor-acceptor interfacial areas can also lead to in charge recombination due to inadequate donor or PC₇₁BM charge percolation pathways.^{100, 101}

In previous studies of the bithiophene imide-benzodithiophene copolymer (PBTIBDT): PC₇₁BM system, addition of 3.0 vol% DIO to the film casting solution significantly increased both the OPV J_{sc} and FF .^{102, 103} To better understand this performance increase, here we analyze the microstructural effects of varying the DIO contents, from 0.0 – 5.0 vol% on solution phase PC₇₁BM and PBTIBDT aggregates using X-ray scattering methods, and relate these changes in aggregate size to the crystalline correlation lengths and domain sizes in the resulting BHJ thin films. Unlike much work in this field, we further relate our morphological findings with charge generation kinetics using transient absorption spectroscopy as a function of the DIO-induced morphology changes. Through

this characterization we are able resolve how these film morphological changes affect electronic processes in the BHJ films at different steps relevant to the OPV function by investigating the initial exciton splitting yields and characterize the free carrier populations from 300 fs to >10 ns after the light excitation. These results provide an incisive, indirect method of probing the mixed regions of the BHJ films and highlight the extent to which processing additives optimize thin film morphology on multiple length scales.

Methods

Materials synthesis. The PBTIBDT synthesis and purification were carried out as previously described.¹⁰² Comparable molecular masses (34 kD) and polydispersities (PDI = 2.3) were obtained. An inverted device structure, ITO/ZnO/PBTIBDT:PC₇₁BM/MoO_x/Ag, was used to characterize solar cell metrics. Pre-patterned ITO substrates (Thin Film Devices, Inc.) with a series resistance of $\sim 8\Omega$ were sonicated sequentially in hexane, DI water, methanol, isopropanol, and acetone for 30 min and then UV/ozone treated (Jelight Co.). Amorphous ZnO layers were deposited via a sol-gel process on the ITO substrates and then annealed in air for 5 min at 150°C. PBTIBDT:PC₇₁BM active layer solutions were prepared in anhydrous *o*-dichlorobenzene (ODCB, Sigma Aldrich, 99.9% purity) with a 1:1.5 w/w ratio of PBTIBDT:PC₇₁BM with a concentration of 10 mg/mL PBTIBDT and heated and stirred 12 h at 60°C to completely dissolve the polymer. When applicable, 1,8-diiodooctane (DIO; Sigma-Aldrich) was added to the active layer solution after 12 h in 1.0 – 5.0 vol%. The active layer solution was then spun-cast at 1250 rpm on the ZnO layer in an N₂ dry box to obtain thicknesses of 100 nm. Thin layers of MoO_x (5 nm) and Ag (100 nm) were subsequently thermally evaporated through a shadow mask at $\sim 10^{-6}$ Torr. The solar cell was encapsulated by a glass slide and UV-curable epoxy prior to testing.

Device characterization. Device J - V characteristics were measured under AM1.5G light (100 mW/cm²) using a Xe arc lamp of a Spectra-Nova Class A solar simulator. The light intensity was calibrated using an NREL-certified monocrystalline Si diode coupled to a KG3 filter to bring the spectral mismatch to unity. Four-point contact measurements were performed and electrical characterizations were measured with a Keithley 2400 unit. The area of all devices was 6 mm².

Solution structural characterization. Solution small-angle X-ray scattering (SAXS) was performed at Beamline 5ID-D at the Advanced Photon Source (APS) at Argonne National Laboratory (ANL). Identical conditions were used to prepare the sample solutions, including neat PBTIBDT solutions, neat PC₇₁BM solutions, and PBTIBDT: PC₇₁BM blend solutions with 0.0–5.0 vol% DIO in ODCB. Solutions were flowed through a 100 μm quartz capillary at 10 μL/s and illuminated with an 8 keV X-ray beam in a 50-μm spot size. Scattering signals without (dark) and with X-ray illumination were collected on two overlapping MAR detectors using a series of ten 3-min exposures, and the corresponding dark data were subtracted from the X-ray illuminated data. Solvent backgrounds were obtained and subtracted from the corrected X-ray illuminated data, and the scattering intensity at given radius was averaged concentrically to yield a scattering trace of intensity vs. scattering vector (q).

Film morphology measurements. Grazing incidence X-ray scattering (GIXS) was performed at Beamline 8ID-E at the Advanced Photon Source (APS) of Argonne National Laboratory. Thin films of the active layer were spun-cast on acetone-cleaned silicon substrates using the same conditions for OPV device fabrication. Thin films were illuminated by the 8-keV X-ray beam at an incidence angle of 0.2° for 10-20 seconds. Data were collected on a 2D Pilatus detector located 204 mm or 1450 mm from the sample for wide-angle and small-angle X-ray scattering, respectively. The location and magnitude of the scattered X-ray beam is described by scattering vector q , which is inversely related to crystalline inter-planar distances, d , by $q = 2\pi/d$. The background scattering was fit to an

exponential decay and subtracted from the data trace for clarity. Line-cuts describing the in-plane and approximate the out-of-plane structure in the film were taken and fit to multiple Gaussians to obtain peak locations and widths.

Atomic force microscopy (AFM) and transmission electron microscopy (TEM) samples were prepared following identical conditions as the actual devices, but TEM samples were drop-cast on PEDOT:PSS coated glass slides. After drying, the substrates were first transferred to DI water and the floated films then transferred to lacey carbon grids (Ted Pella, Inc.). TEM images were obtained on JOEL JEM-2100 TEM. AFM measurements were performed on a Dimension Icon Scanning Probe Microscope (Veeco) in tapping mode.

Transient optical absorption spectroscopy. Femtosecond transient absorption (fs TA) measurements were performed with an apparatus based on an amplified Ti-Sapphire laser system (Spitfire Pro XP). Here a 10 kHz, amplified 830 nm beam with energy of 3 mJ was generated by a Spitfire Pro XP regenerative amplifier (Spectra Physics Lasers). The Spitfire Pro XP was pumped by an Empower Nd:YLF laser (Spectra Physics Lasers) with a seed beam generated by a Mai Tai Ti:sapphire oscillator (Spectra Physics Lasers). Most of the 830 nm amplifier output is used to run a home-built, white light-seeded OPA to create the pump beam while a small percentage of the 830 nm amplifier output is used to create the white light probe. The white light probe was generated in the Helios (Ultrafast Systems) by focusing on a thin disk of sapphire for visible detection or an IR crystal. The pump wavelength was tuned to 540-580 nm with an energy of 20 μ W and chopped at 500 Hz to generate the difference spectrum. At the sample, the pump beam was focused to 100 μ m diameter with an instrument response function of 240 fs, yielding a fluence of 30 μ J/cm². The white light probe was dispersed onto a CCD camera with an integration time of 3 sec per spectrum. Experiments were conducted at 25°C under an N₂ flow. Typically 5 - 6 scans were averaged and samples were moved between scans to minimize photodegradation.

Single wavelength kinetic traces in the 5 ns– 80 μ s range were also recorded. Samples were pumped at 540 nm using the output of an optical parametric oscillator pumped with the third harmonic of a NdYAG laser (Surelite-II, Continuum). The pump pulse width was approximately 5 ns. Single wavelength kinetic traces were probed using a single wavelength 1070 nm LED operated in pulsed mode with a 0.1% duty cycle and a 200 ps pulse width (Thor labs). Spectra were detected by a biased InGaAs PIN diode (ET-3040) from Electro-Optic Technology. The diode output was digitized with a Picoscope 4227 (250 Ms/s sampling rate, 12-bit).

Results

Based on the observed variation in OPV performance with 0.0 – 5.0 vol% DIO solvent additive, we focus on understanding those factors underlying performance variations through studies of the active layer solution and thin film morphology using X-ray scattering, AFM, and TEM, as well as correlations of morphology with exciton generation and charge transport dynamics, measured with optical fs and ns transient absorption spectroscopy. It will be seen that DIO addition reduces the PC₇₁BM solution aggregate size, promoting the formation of interpenetrating donor and PC₇₁BM BHJ domains, leading to larger initial PBTIBDT cation populations. However, the resulting variations in PC₇₁BM interconnectivity have a major impact on the resulting solar cell performance.

Solar cell performance. PBTIBDT:PC₇₁BM solar cells were fabricated using 0.0 – 5.0 vol% DIO solvent additive in the active layer solution prior to spin-coating (Figure 1). The highest PCE of 5.36% is achieved using 3.0 vol% DIO with $V_{oc} = 0.959$ V, $J_{sc} = 8.87$ mA/cm², and $FF = 65.7\%$ (Table 1). Devices fabricated with 2 vol% DIO exhibit slightly lower PCEs (5.27%) attributed primarily to decreased J_{sc} of 8.38 mA/cm². Cells processed without DIO afford the lowest PCE = 2.82% with both the $J_{sc} = 6.00$ mA/cm² and $FF = 51.8\%$ depressed. Variations in V_{oc} are the result of standard variations in solar cell fabrication steps, leading to variation of ± 0.02 eV.¹⁰⁴

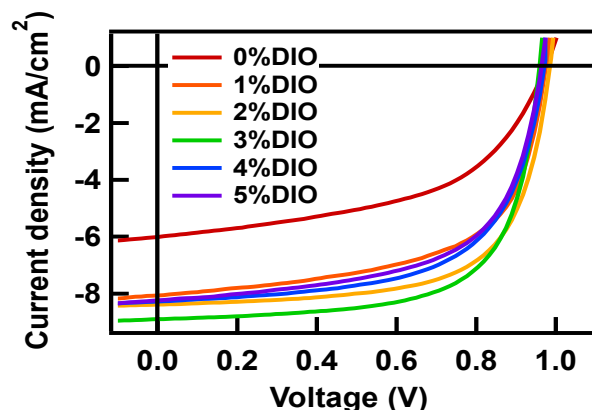


Figure 1. *J-V* response of PBTIBDT:PC₇₁BM solar cells with varying concentrations of DIO in the *o*-dichlorobenzene film casting solution.

Table 1. Performance metrics of PBTIBDT:PC₇₁BM solar cells fabricated with varying concentrations of DIO in the *o*-dichlorobenzene film casting solution.

[DIO] (%)	V_{oc} (V)	J_{sc} (mA/cm ²)	FF (%)	PCE_{max} (%)	PCE_{avg} (%) ^a
0	0.973	6.00	51.8	3.03	2.82
1	0.973	8.06	60.6	4.75	4.59
2	0.987	8.38	65.2	5.48	5.27
3	0.959	8.87	65.7	5.59	5.36
4	0.973	8.28	61.9	4.99	4.81
5	0.959	8.23	61.2	4.83	4.56

^aMeasured over 8-10 devices.

Aggregate dimensions in solution. To understand the origin of the BHJ thin film morphology differences, the aggregation properties of PBTIBDT and PC₇₁BM (if any) in *o*-dichlorobenzene with 0.0 – 5.0 vol% DIO were analyzed by small angle X-ray scattering (SAXS). Data were fit using a Unified fit procedure¹⁰⁵⁻¹⁰⁷ in which the scattering signal trace is simultaneously fit using Guinier and Porod models for small spherical non-interacting particles in a uniform matrix. The particle radius of gyration (R_g) is determined by the location and bend in the “Guinier knee,” while the slope after the knee, the Porod region, is characteristic of the particle surface texture and dimensionality.¹⁰⁸

The PBTIBDT solution traces exhibit a fall in intensity as a function of the scattering factor Q from $Q = 0.007 \text{ \AA}^{-1}$ with a slight Guinier knee in the trace around $Q = 0.007 - 0.03 \text{ \AA}^{-1}$ for all samples, and a second knee at $0.03 - 0.07 \text{ \AA}^{-1}$ (Figure 2A) indicating the presence of two types of PBTIBDT aggregates. Fitting the low Q Guinier knee reveals that this first population of PBTIBDT aggregates with 1.0 – 5.0 vol% DIO have a R_{g1} of $49.1 \pm 1.2 \text{ \AA}$ to 43.5 ± 0.9 while PBTIBDT with no DIO has an $R_{g1} = 78 \pm 3.5 \text{ \AA}$ (Table 2). The second Guinier knee yields R_{g2} values of $9.3 \text{ \AA} - 10.8 \text{ \AA}$ with no

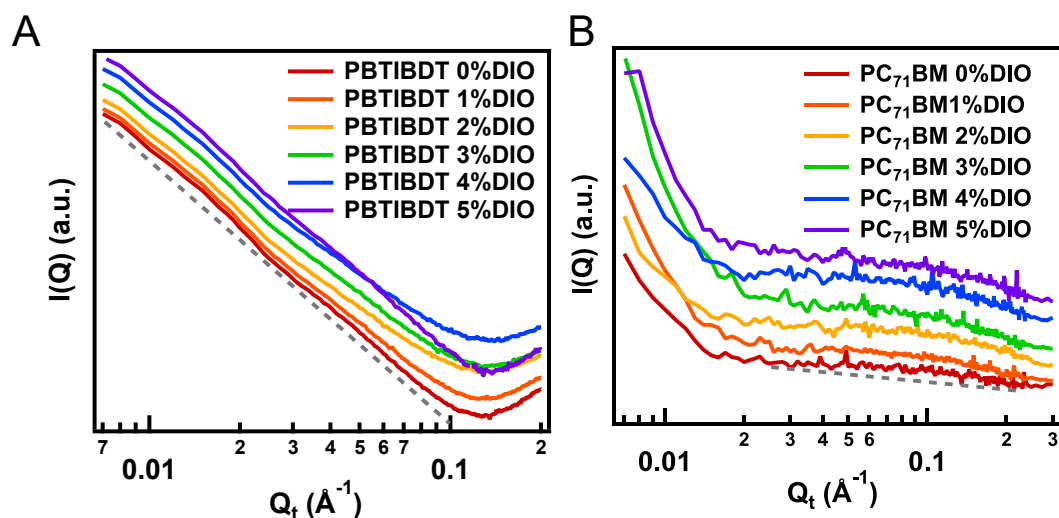


Figure 2. Solution phase small angle X-ray scattering traces of, (A) PBTIBDT and (B) PC₇₁BM in *o*-dichlorobenzene solution with 0.0 – 5.0% DIO used to estimate aggregate size. Straight gray dotted lines provide visual guidance to peak locations and traces are offset for clarity.

trend in R_{g2} with vol % added DIO. This large initial decrease in R_{g1} aggregate size was not present in the previously studied PTB7 system (Figure 1)⁷⁸, but is likely attributable here to solubilization by the side chain substituents of loosely bound PBTIBDT aggregates which would exhibit tighter packing in neat ODCB.⁵⁸ Unlike PTB7, the large branched 2-hexyldecyl and *n*-dodecyl side chains of PBTIBDT may contribute to the early solubility on incremental DIO addition. The slight fall in PBTIBDT R_{g1} with a 1.0 to 5.0 vol% DIO increase suggests the continued DIO interaction with

loosely aggregated PBTIBDT segments while the constant size of the PBTIBDT R_{g2} aggregates suggests that they may be more strongly aggregated than the R_{g1} aggregate distribution.

Table 2. Solution phase radii of gyration (R_g) of neat PBTIBDT and PC₇₁BM aggregates in *o*-dichlorobenzene with 0.0 – 5.0 % DIO obtained from SAXS measurements.^a

[DIO] (%)	PBTIBDT R_{g1} (Å)	PBTIBDT R_{g2} (Å)	PC ₇₁ BM R_g (Å)
0	78.0 (3.5)	10.6 (0.8)	17.0 (2.0)
1	49.1 (1.2)	10.8 (0.2)	15.9 (2.2)
2	46.1 (1.1)	10.7 (0.6)	11.9 (1.6)
3	45.9 (1.0)	10.6 (0.2)	8.8 (0.7)
4	45.9 (1.1)	10.4 (0.2)	10.0 (1.1)
5	43.5 (0.9)	9.3 (0.7)	11.6 (1.0)

^aQuantities in parentheses are estimated uncertainties from the Unified fitting procedure.

The neat PC₇₁BM traces in *o*-dichlorobenzene exhibit an initial sharp drop in intensity from $Q = 0.007$ to 0.02 \AA^{-1} followed by a slightly visible Guinier knee (Figure 2B). The DIO concentration dependence of the PC₇₁BM aggregate size is evident from the decrease of the slope of the scattering intensity $I(Q)$ vs. Q , as well as the Q value as a function of the DIO concentration. Indeed, a decrease in PC₇₁BM R_g from $17.0 \pm 2.0 \text{ \AA}$ to $8.8 \pm 0.7 \text{ \AA}$ for 0.0 – 3.0 vol% DIO and then an unexpected rise in PC₇₁BM R_g to 11.6 \AA with 5.0 vol% DIO (Table 2) is observed. Since $R_g = 8.8 \text{ \AA}$ corresponds to 1-2 PC₇₁BM molecules, it is conceivable that after fully solubilizing all of the PC₇₁BM molecules, the solubilized PC₇₁BM molecules begin to re-aggregate inside DIO-rich solvation domains as the DIO concentration increases further. Fits of the PBTIBDT: PC₇₁BM blend solutions yield similar domain sizes, and traces can also be fit using a linear combination of neat PBTIBDT and PC₇₁BM traces, indicating that the PBTIBDT and PC₇₁BM aggregates are not strongly interacting (see Supporting Information).

Crystal Structure and Domain Size in the Thin Films

TEM images of films spun-cast from *o*-dichlorobenzene solutions with zero and 1.0 vol% DIO exhibit large dark domains (~80 nm) distributed in a matrix of lighter colored domains (Figure 3). Using energy dispersive X-ray spectroscopy (EDS), it can be determined that the darker regions have higher concentrations of PC₇₁BM. As the concentration of DIO is increased to 2.0 – 5.0 vol%, mixed film morphologies are observed in which the PC₇₁BM appears to be evenly dispersed throughout the film. However, TEM can only provide a relative contrast indicative of discrete domains, and shows no obvious morphology differences between the 2.0 – 5.0 vol% DIO films.

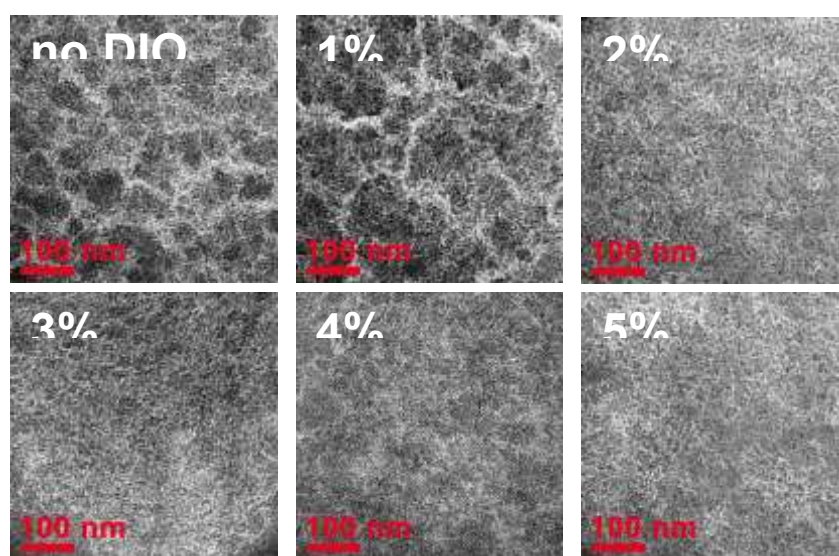


Figure 3. TEM images of PBTIBDT: PC₇₁BM blend films cast from *o*-dichlorobenzene with 0.0-5.0 vol% DIO. The darker regions have higher PC₇₁BM concentrations.

Grazing incidence X-ray scattering was next used as a complement to TEM for characterizing the film PBTIBDT packing and domain sizes. From grazing incidence wide-angle X-ray scattering (GIWAXS), the crystalline inter-chain π -stacking distances and lamellar d -spacings as well as crystalline correlation lengths for neat PBTIBDT films, neat PC₇₁BM, and PBTIBDT: PC₇₁BM blend films with 0.0 – 5.0 vol% DIO can be determined (Figure 4). The average lamellar d -spacing determined by the q values of the scattering feature corresponding to PBTIBDT side chains is 27.4 ± 0.8 Å in the neat film and falls slightly to 25.4 ± 0.3 Å in the blend film. The lamellar scattering reflection is isotropic, but is more intense in the in-plane scattering orientation, indicating that the

polymer is largely “ π -face-down” with the π -conjugated backbone parallel to the substrate (Figure 4B). The PBTIBDT π - π stacking distance determined by the feature at $q_z = 1.75 \text{ \AA}^{-1}$ is consistently 3.6 \AA in the neat and blend films. Since the π - π stacking reflection appears more strongly in the out-of-plane scattering, this confirms that the ordered portion of the polymer, most likely to be near the interface with the electrode surface, has a π -face-down orientation on the substrate. All lamellar

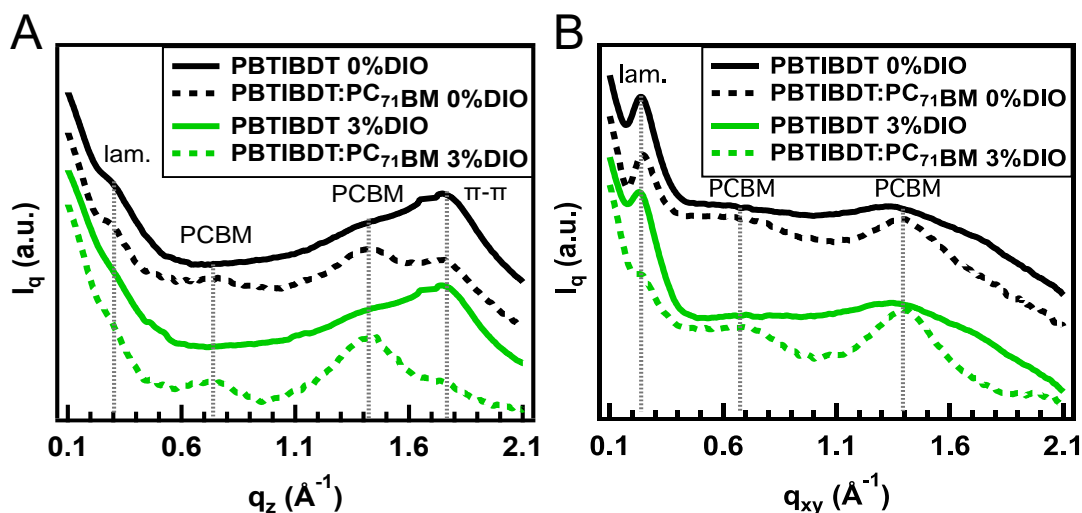


Figure 4. Morphology and crystal structures of neat and blend PBTIBDT films cast from *o*-dichlorobenzene with 0.0 and 3.0 vol% DIO as described by GIWAXS line-cuts in the, (A) out-of-plane orientation and (B) in-plane orientation describing the crystal structure and crystalline correlation lengths.

d -spacings in the neat and blend films are within a 5% margin of error, so it is concluded that DIO addition has a negligible effect on the PBTIBDT packing (see Supporting Information). In neat and blend films and at all concentrations of added DIO, PC₇₁BM exhibits an isotropic ring at $q_z = 1.4 \text{ \AA}^{-1}$ corresponding to a d -spacing of 4.5 \AA .

Table 3. Thin film domain sizes calculated by a Guinier fit to the GISAXS data, and crystalline correlation lengths calculated by Scherrer analysis of GIWAXS data. Errors in fit given in parentheses.

[DIO] (%)	Crystalline correlation length (nm)					Domain size (nm)	
	PBTIBDT			PC ₇₁ BM		PBTIBDT	PC ₇₁ BM
	lam. (neat)	lam. (blend)	π - π (neat)	neat	blend		
0.0							
3.0							

0	7.9 (0.1)	7.7 (0.1)	3.0 (0.0)	3.3 (0.2)	2.8 (0.0)	21.7 (3.9)	4.5 (0.4)
1	7.0 (0.2)	7.1 (0.1)	3.1 (0.0)	3.6 (0.1)	3.1 (0.4)	14.8 (2.2)	7.8 (0.9)
2	8.0 (0.1)	7.2 (0.3)	3.3 (0.3)	2.6 (0.0)	3.1 (0.2)	14.6 (4.2)	5.2 (2.2)
3	6.7 (0.2)	5.9 (0.1)	3.2 (0.0)	3.3 (0.0)	2.8 (0.0)	14.6 (6.6)	5.9 (0.7)
4	6.6 (0.1)	8.9 (0.3)	2.9 (0.0)	4.0 (0.2)	3.0 (0.1)	16.5 (7.2)	5.8 (1.4)
5	6.2 (0.1)	7.1 (0.2)	3.2 (0.0)	3.5 (0.4)	2.8 (0.3)	14.3 (5.1)	5.7 (1.9)

Using a modified Scherrer analysis,¹⁰⁹ trends in crystalline correlation length along a given diffraction plane can be extracted. The basic Scherrer equation $D_{hkl}=2\pi K/\Delta d_{hkl}$ relates the correlation length of a given diffraction peak, D_{hkl} , to the full width half-maximum of the diffraction peak, d_{hkl} . K is a constant related to the crystalline domain shape and the commonly accepted $K = 0.9$ for spherical polymer crystalline domains¹⁰⁹ was used here. Note that the Scherrer analysis does not account for peak broadening arising from crystalline disorder, so it estimates a minimum crystalline correlation length, and it is reasonably assumed that the internal disorder within the crystal remains the same for all PBTIBDT and PC₇₁BM films. In neat PBTIBDT films, the lamellar crystalline correlation length decreases from 7.9 nm to 6.2 nm as the DIO concentration is increased, mirroring the trend seen in the solution SAXS results (Table 3). A similar decrease is not evident in the blend PBTIBDT:PC₇₁BM films, and the domain sizes vary from 5.9 – 8.9 nm, averaging 7.6 nm with no apparent correlation with DIO vol%. There is no significant change in the π - π stacking correlation length which is 3.3 nm in the neat film. We were not able to confidently determine the correlation length in the blend film due to the overlap of the PC₇₁BM ring and π - π stacking peaks. Neat PC₇₁BM films were also examined by GIWAXS as a function of added DIO. The d -spacing remains constant in the neat and blend films, indicating that DIO does not significantly affect the PC₇₁BM packing (see Supporting Information). Interestingly, the films exhibit no consistent change in crystalline correlation length with different DIO concentrations in the neat (2.6 – 3.9 nm) or blend (2.8 – 3.1 nm)

films, but generally the PCBM domain size decreases by ~ 0.5 nm from the neat to blend film for a given vol% DIO.

The grazing incidence small angle X-ray scattering (GISAXS) domain size measurement is sensitive to electron density differences, and therefore is used here to determine the size of both amorphous and crystalline domains in a given material. Importantly, GISAXS measurements complement the Scherrer analysis from the above GIWAXS data analysis which estimates the size of only the crystalline domains. Because GISAXS depends on electron density contrast, we are only able to measure the domain sizes in the blend films, and the GISAXS traces were fit to two particle size distributions which can be related to the PC₇₁BM and PBTIBDT domains based on the crystalline correlation lengths and solution SAXS measurements of aggregate sizes (Figure S5). From these data, it is only possible to conclude that the larger domains are predominately BTIBDT since they exhibit a different electron density than the mixed phase and pure/predominantly PCBM regions of the film. The radius of gyration (R_g) was determined using the same Unified fitting procedures as for the solution SAXS.¹⁰⁵⁻¹⁰⁷ As expected, the domain sizes measured by GISAXS are consistently larger than those from the Scherrer analysis because the GISAXS domain size includes non-crystalline regions. The initial decrease in PBTIBDT GISAXS domain size from 21.7 nm to 14.8 nm upon 1.0 vol% DIO addition mirrors the decrease in aggregate radius seen in the solution phase SAXS measurements. This decrease indicates formation of denser PBTIBDT domains due to increased side chain organization and/or expulsion of included PC₇₁BM molecules. A slight increase in PC₇₁BM domain size is observed on 1.0 vol% DIO addition, suggesting that DIO addition promotes the formation of more pure PBTIBDT domains and a concurrent increase in the size of the pure PC₇₁BM domains. However, the PC₇₁BM domain size is essentially unchanged for 2.0 – 5.0 vol% DIO at ~ 5.7 nm, indicating that the PBTIBDT domain purity is constant for films with 1.0 – 5.0 vol% DIO.

Exciton and Charge Generation/Transport Dynamics by Optical Transient Absorption Spectroscopy. Although it is well-known that the BHJ film morphology affects the OPV performance metrics, it is not clear how the film morphology in the present system affects the exciton splitting dynamics and yields. Optical transient absorption (TA) spectroscopy on both ultrafast (0 – 3 ns) and longer (5 ns to 20 μ s) time scales enables monitoring of the time-dependent populations of various intermediate species, such as the exciton (EX) and charge-separated (CS) states, as well as the ground state bleach/recovery (GSB) following light absorption.^{110, 111} From these measurements, the charge-separated state populations and charge-separation/recombination kinetics can be extracted.¹¹² We focus here on the near-infrared (NIR) spectral region, where these intermediate states absorb after being created by photoexcitation at 630 nm, the peak absorption of the polymer (spectra available in SI). In this system, the CS state spectral signature is represented by the TA spectral signal of the polymer cation (CAT), obtained independently from spectroelectrochemical measurements (see SI).

NIR and visible fs TA was performed on dilute air-free PBTIBDT solutions in *o*-dichlorobenzene to first determine the EX signal location and the intrinsic EX decay dynamics in the absence of the PC₇₁BM acceptor. The solution NIR TA spectra at a delay time of 1 ps exhibit a broad signal spanning 1000-1400 nm (Figure 5A). Although these TA features are very broad due to the BHJ film inhomogeneous local environment and structural diversity, the central positions of the different species can be confidently assigned by scrutinizing the TA spectral evolution with the delay time. By capturing the earliest delay time TA spectra of the polymer in solution and in the neat films, the EX spectral feature centered around 1040 nm can be assigned because it is the feature emerging at the earliest when the CAT still has a very low concentration. The CAT spectral feature is assigned to the peak centered around 1180 nm, based on the results from spectroelectrochemistry (see SI). The delay time dependent EX peak intensity was next used to extract the solution phase exciton dynamics

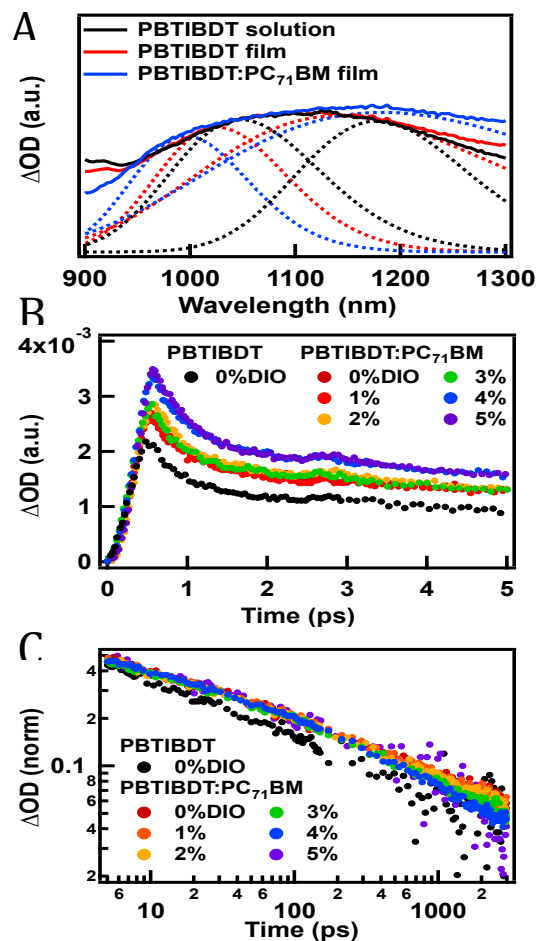


Figure 5. Transient absorption spectra of (A) PBTIBDT solution in *o*-dichlorobenzene, PBTIBDT neat film with 0.0 vol% DIO, and PBTIBDT: PC₇₁BM film with 3.0 vol% DIO at 1 ps after excitation, showing the underlying exciton and cation peaks at $\lambda = 1000$ – 1040 nm and 1180 nm, respectively, (B) initial cation population and decay normalized to the ground state bleach signal amplitudes, (C) decay of the cation peak at 1180 nm with different DIO concentrations.

of PBTIBDT, which were later used references to determine the thin film exciton dynamics. The fitting was carried out by dual Gaussian functions centered at each delay time, and the integrated area under the Gaussian function as a function of delay time was used to extract the kinetics for both EX and CAT (see SI for full details). The CAT formation in solution phase for the charge transfer polymers have been observed in PTB7, which was attributed to polymer self-folding/aggregation where the inter-segment within a polymer chain facilitate the CS state formation without the presence of the acceptor at much lower yields.¹¹³

NIR transient absorption spectra at 1 ps time delay of the neat PBTIBDT films with 0.0, 3.0, and 5.0 vol% DIO, and of PBTIBDT: PC₇₁BM blend films with 0.0 – 5.0 vol% DIO exhibit a broad feature encompassing two peaks, the locations and widths of which were determined from a Gaussian multi-peak fit (Fig 5A).¹¹⁴ This analysis reveals two peaks: a broad peak centered ~1140 nm (neat films) or ~1180 nm (blend films) and a narrower feature centered at ~1000 nm for both the neat and blend films. From thin film spectroelectrochemistry, the cation absorption feature in PBTIBDT films is a broad absorption extending from 950 nm into the NIR. The previously observed lack of a red-shift in the PBTIBDT ground state absorption from solution to films indicates that the polymer is significantly aggregated in ODCB solution, so similarity in EX peak location from solution to thin films is expected. Therefore, the narrow peak at 1000 nm is assigned to EX absorption and the broad feature at 1140/1180 nm to CAT absorption. The increase in intensity of the 1180 nm peak with PC₇₁BM addition further supports the 1180 nm peak assignment to the cation. Kinetic traces at 1180 nm were normalized with respect to the ground state bleach intensity at 1 ps (see SI) and show that the initial cation population is highest for blend films processed with 4.0 – 5.0 vol% DIO and 25% lower for films processed with 0.0 – 3.0 vol% DIO (Figure 5B). As expected, neat PBTIBDT film exhibits the smallest initial cation population.

Despite the variation in normalized initial CAT population at different DIO concentrations, the CAT decay kinetics of the neat PBTIBDT films remain invariant, so the CAT dynamics of the 0.0 vol% DIO film are used here as the PBTIBDT standard for later comparisons. The EX (see SI) and CAT signals (Figure 5C) were fit using a sum of three exponential decay functions while the recovery of the GSB signal in the visible region (see SI) was fit using a sum of four exponential rise functions (recovery). The EX signal exhibits three lifetimes: 1) <1ps (τ_1) attributed to ultrafast exciton splitting and any possible exciton-exciton annihilation process; 2) 4 ps (τ_2) attributed to internal conversion because the ground state recovery kinetics also show a corresponding time constant, and 3) >3 ns (τ_4)

accounting for a small portion (6%) of the long-lived exciton population. The kinetics of the CAT peak exhibit a ~ 100 ps decay (τ_3) due to charge recombination and a long lived cation species (τ_4) which can only be determined using ns flash photolysis as shown below (Table 4). Due to the global fitting procedure used, τ_2 is only observed in the EX decay while τ_1 (see SI) is attributed to EX-CAT or CAT-CAT annihilation arising from the high pump power used. The GSB kinetics show rise times corresponding to the EX decay ($\tau_2 = 4$ ps) and CAT decay ($\tau_3 = 100$ ps) as well as a long-lived GSB signal due to processes with long (>3 ns) time constants, such as triplet exciton decay, free carrier generation, etc.¹¹⁵ In the present data analyses, the three signals are globally fit using unified

Table 4. Fitting parameters of PBTIBDT: PC₇₁BM cation signal at 1180 nm showing decay rates (τ) and relative fractions (p^*) from the population remaining after 1 ps. The relative fractions (p) of the total and τ_1 are presented in the SI. τ_2 is only associated with the EX feature.

[DIO] (%)	τ_3 (ps)	p_3^* (%)	τ_4 (ps)	p_4^* (%)
0 (neat)	61 (10)	89 (8)	<3000	11 (4)
0	97 (8)	84 (4)	>3000	16 (2)
1	92 (10)	86 (5)	>3000	14 (2)
2	70 (10)	84 (5)	>3000	16 (2)
3	65 (11)	85 (6)	>3000	15 (3)
4	71 (5)	87 (2)	<3000	13 (1)
5	50 (8)	87 (4)	<3000	13 (2)

time constants, linking the ESA signal (τ_1), the exciton decay/GSB rise (τ_2), and the cation decay/GSB rise (τ_3) while the amplitudes of the decays are allowed to vary. A fourth exponential component with an apparent $\tau_4 \sim 3$ ns was also included, but not linked for any component due to its uncertainty in the delay time window of the fs optical TA setup. Due to broadening of the CAT signal in the blend film, it was not possible to fit the EX decay with only the <1 ps, 4 ps, and >3 ns decay rates. Therefore, τ_3 is linked to the CAT decay in the global fitting procedure. Fitting parameters of the EX and GSB signals are provided in the SI.

The relevant cation decay rates and their corresponding relative fractions of the cation population (Table 4) indicate longer cation lifetimes in blend films than in the neat films. This is expected since PC₇₁BM can extract electrons from the polymer with a much larger driving force than the intrinsic polymer exciton splitting. Interestingly, as the DIO concentration is increased in the blend films, the charge recombination time constant characterized by τ_3 (Table 4) decreases from 97 ps to 50 ps with the largest difference between films with 1.0 and 2.0 vol% DIO, although the relative ratio to the long time constant is unchanged, 1:8-9. The long-lived cation lifetime (τ_4) is fit only approximately due to time window limitations, however films with 4.0 – 5.0 vol% DIO have shorter lifetimes (<3000 ps) and slightly smaller long-lived cation populations than films with 0.0 – 3.0 vol% DIO. To determine the longer lifetimes of the cation species, samples were studied using ns TA at a probe wavelength of 1070 nm where the exciton intensity is minimized and the cation feature is still present.

Table 5. Fitting parameters for cation decay at 1070 nm for long time delays (5 ns – 20 μ s).^a

[DIO] (%)	τ (ns)^a
0 (neat)	65 (4)
0	56 (3)
1	53 (3)
2	54 (2)
3	44 (4)
4	64 (3)
5	62 (3)

^aNumbers in parentheses are estimated fitting uncertainties

Kinetic curves for the thin films at the 1070 nm probe wavelength at early times (5 – 200 ns) (Figure 6; Table 5) show a strong DIO concentration dependence in the total signal intensity, corresponding to the population of cation charge carriers while there are no significant changes in decay rate constants. This result indicates that the highest total intensity or the highest cation population is

observed in films processed with 2.0 – 3.0 vol% DIO, however the signal intensities are ~30% lower with 0.0 – 1.0 vol% DIO and ~40% lower with 4.0 – 5.0 vol% DIO. Despite a smaller initial cation population observed at 1 ps for films with 2.0 – 3.0 vol% DIO (Figure 5B), at a 5 ns delay

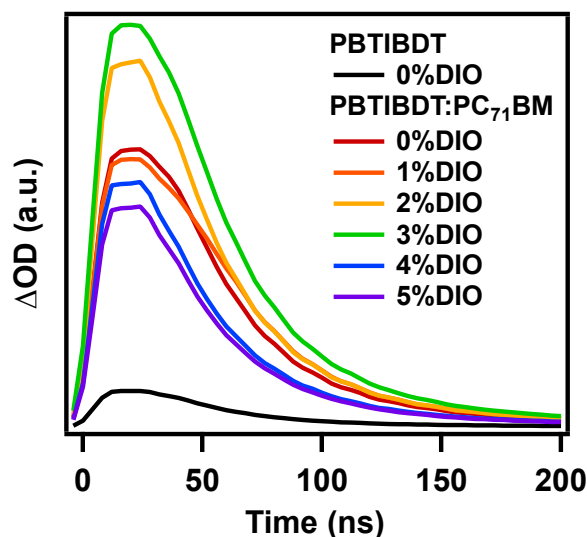


Figure 6. Long-lived cation populations in PBTIBDT and PBTIBDT: PC₇₁BM thin films as measured by ns TA.

time they have the largest long-lived cation population. The kinetic traces were fit by a single exponential function, neglecting a long-lasting signal with < 4% contribution.

Discussion

Based on results for 150 BHJ OPV systems reported in the literature, we recently argued that while the driving force for exciton splitting and the optical band gap correlate poorly with device PCE, both J_{sc} and FF correlate strongly with PCE and are influenced by the DIO used in active layer fabrication.³¹ J_{sc} is a measure of charge collection efficiency resulting from multiple processes including light absorption, charge separation, and charge recombination,^{3, 116} while FF is primarily a measure of carrier recombination;^{117, 118} nevertheless both metrics are highly morphology-dependent. The present study provides detailed characterization and a direct link between active layer morphology and polymer cation kinetics and yields, demonstrating that charge separation and

recombination are predominantly morphology-driven given the large driving force (0.6 eV) for exciton splitting in this system. The focus here is to elucidate the specific roles of DIO by assessing the correlations between film morphology, modulated by the different DIO concentrations, and the exciton and charge carrier dynamics at different stages of OPV function.

Influence of DIO on active layer morphology. From the solution X-ray analysis, a decrease in PC₇₁BM aggregate size is observed on addition of 0.0 – 3.0 vol% DIO, followed by a slight increase at 4.0 – 5.0 vol% DIO, so it is noteworthy that no corresponding decrease and rise in film PC₇₁BM domain size is observed over these two DIO concentration ranges. However, from the PBTIBDT:PC₇₁BM blend film TEM images, a decrease in the PC₇₁BM-rich region sizes is observed (Figure 3), indicating increased PC₇₁BM dispersion throughout the film. Therefore, the principal effect of DIO in this system is the dissolution of PC₇₁BM aggregates in solution to enable the formation of a larger percentage of intermixed polymer + PC₇₁BM networks as well as the formation of smaller pure PC₇₁BM domains. This concurrent presence of a range of mixed phases at length scales of < 50 nm is considered crucial to increasing charge generation and decreasing charge recombination and is linked to the increased FF and J_{sc} .^{65, 79, 80, 88} Figure 7A presents a schematic of the PBTIBDT: PC₇₁BM interfacial morphology with no DIO where there are large segregated PBTIBDT-rich and PC₇₁BM-rich domains, resulting in small PBTIBDT-PC₇₁BM interfacial areas, but well-connected PBTIBDT and PC₇₁BM charge percolation pathways. At the other extreme, PBTIBDT: PC₇₁BM films with 5.0 vol% DIO form an interpenetrating texture at the interface resulting in high PBTIBDT-PC₇₁BM interfacial area, but also leading to charge-trapping PC₇₁BM islands. However, films with 3.0 vol% DIO afford mixed textures, enhancing interfacial area versus films with no DIO, while maintaining charge percolation pathways through pure PBTIBDT and PCBM domains. In addition, the small crystalline correlation length of PCBM and BTIBDT in the 3.0 vol% DIO thin film can mediate charge transport through the pure domains and mixed phase

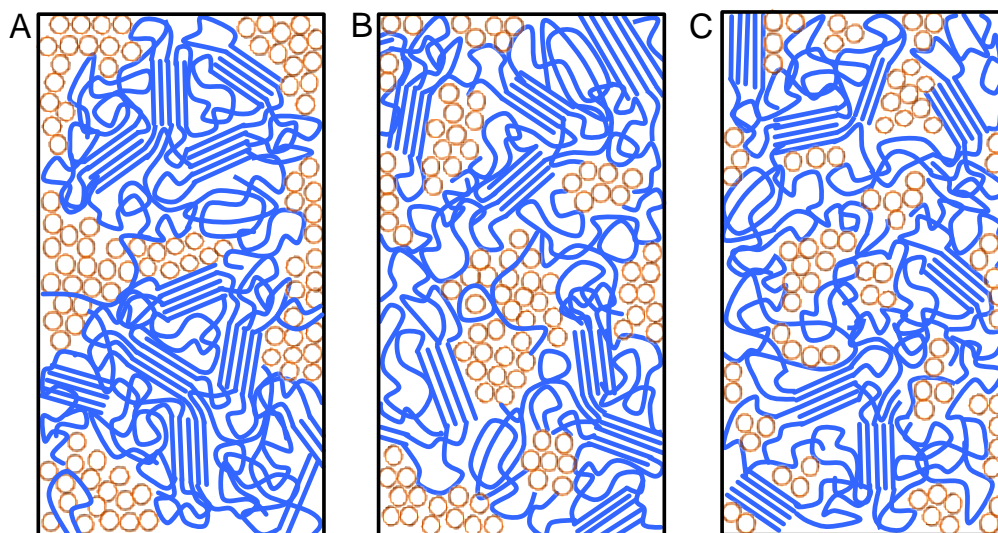


Figure 7. Schematic of the packing morphology of the *interfacial region* of PBTIBDT: PC₇₁BM blend films processed with, A) no DIO, B) 3.0 vol% DIO, and C) 5.0 vol% DIO. PBTIBDT polymer chains are shown in blue and PC₇₁BM molecules are shown in orange. As vol% DIO is increased, PBTIBDT domains become more loosely packed and PC₇₁BM aggregate size decreases, allowing increased PC₇₁BM intermixing.

regions while the increasing purity of the BTIBDT domains measured by GISAXS enhances hole transport. Note that the 3.0 and 5.0 vol% DIO films also contain pure PBTIBDT and PCBM domains (not shown in the interfacial region of Figure 7) as evidenced by the X-ray scattering results in Table 3, but the focus here is on the donor-acceptor interface where charge generation and recombination occur.

Morphology-dependent dynamics of intermediate species The effects of mixed phases and the resulting changes in interfacial area and percolation pathways in the thin films were investigated here by measuring the relative charge-separated state populations. The most striking observation is the DIO concentration dependence of the initial and long time CAT yields, and the lack of DIO concentration dependence on the time constants for the decays of the various intermediate species, a trend that was also observed in PTB1:PCBM BHJ films (note: PTB1 is a derivative of PTB7 without F atoms).¹¹⁹ These results are at first puzzling using models which associate long exciton splitting times with larger domain sizes.^{94, 120} However, the present X-ray scattering results show that all domain sizes in the PBTIBDT: PC₇₁BM blend films are rather small with dimensions of ~20 nm. This quantity can be somewhat misleading since the polymer packing is significantly disordered with

the majority of structures invisible to X-ray diffraction. Therefore, in this particular polymer system, the insensitivity of the kinetics to the domain size suggests that the dominant exciton splitting takes place in interpenetrating small donor - acceptor boundary regions with negligible exciton diffusion. The sensitivity of the cation production yield to the domain size simply reflects donor-acceptor interfacial area changes as the domain sizes are adjusted by the amount of DIO present during film fabrication. The trend in the initial CAT population mirrors the increase in donor-accepter interfacial area as the concentration of DIO is increased. The initial CAT population after the exciton splitting is greatest for films processed with 4.0 – 5.0 vol% DIO, decreases ~25% for films with 1.0 – 3.0 vol% DIO, and decreases further for films having no DIO. As expected, neat PBTIBDT films exhibit the smallest initial cation population.

To determine how the initial PBTIBDT cation populations evolve over time scales longer than a few ns, the cation population surviving geminate charge recombination was measured. Ultimately, the cation and electron populations over the long timescale after exciton splitting are most likely responsible for the OPV J_{sc} and hence PCE. Note that PBTIBDT:PC₇₁BM films processed with 2.0 – 3.0 vol% DIO exhibit larger cation populations than films with 0.0 – 1.0 vol% DIO, and films with 4.0 – 5.0 vol% DIO display the smallest cation population. Compared to the initial cation population increase, trends with DIO concentration on the ps timescale, the cation population on the ns - μ s timescale differs and reflects the interplay between initial cation generation and cation transport away from interfacial recombination sites. Despite the formation of the largest CS population in the active layer at 1 ps delay for 4.0 – 5.0 vol% DIO concentration, the cation population that survives on the μ s timescale is the lowest due to the small film PC₇₁BM domain sizes and overmixing, leading to enhanced charge recombination. In contrast, the larger domain sizes in films with 0.0 – 1.0 vol% DIO suppress recombination and promote relatively larger, long-lived cation populations. In particular, the combination of a moderately large initial (1 ps) cation population for films with 2.0 –

3.0 vol% DIO and adequately separated domains, results in the largest long-lived cation populations in these PBTIBDT: PC₇₁BM films. Since cations with longer lifetimes have a higher probability of charge collection, the larger long-lived cation population in the present films with 2.0–3.0 vol% DIO correlates with the relatively high observed J_{sc} and FF values.

Ade and coworkers previously linked the average purity of phases with <50 nm length scales to J_{sc} and FF . He found that films with a lower average purity at <50 nm lengths scales have increased FF and J_{sc} , attributed to improved charge transport mediation between the pure and finely mixed phases.⁸⁰ In this investigation, we draw a similar comparison between PC₇₁BM aggregate size in solution and J_{sc} and FF in thin BHJ films (Figure 8). Since the PC₇₁BM aggregate size in solution is shown to have no effect on the PC₇₁BM domain size in thin films, we conclude that the primary contribution of DIO is to enhance PC₇₁BM mixing in the film mixed phase regions. In the present BHJ system, J_{sc} is more strongly correlated with PC₇₁BM solution aggregate size than FF . Since J_{sc}

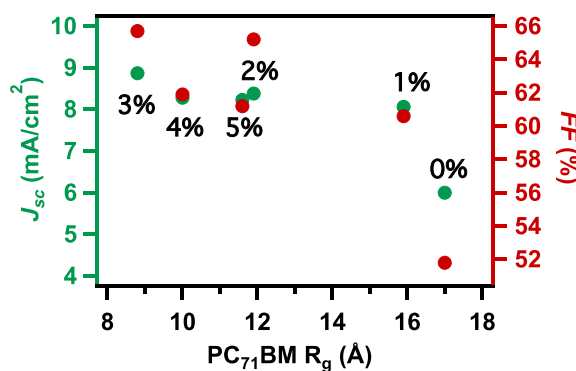


Figure 8. Increase in J_{sc} and FF as PC₇₁BM solution aggregate size decreases with increasing vol% DIO

is dominated by charge generation while FF is primarily limited by recombination events, this suggests that the present solar cells without DIO are limited in performance by low charge generation due to the small PBTIBDT-PC₇₁BM interfacial area. With DIO addition, J_{sc} increases concurrent with an increase in the 1 ps initial cation population. This change in initial population is reasonably attributable to increased interfacial area formed by small PC₇₁BM aggregates in solution which then

penetrate into the polymer matrix, creating mixed phase regions. A similar rise in FF is observed for 0.0 – 3.0 vol% DIO, while a fall in FF is seen for 4.0 – 5.0 vol% DIO. The initial increase can be attributed to enhanced charge separation and transport due to the formation of smaller and more pure PBTIBDT and PCBM domains in the 0.0 – 3.0 vol% DIO regime, while films with 4.0 – 5.0 vol% DIO trend towards mixed phase morphologies, leading to PC₇₁BM islands which trap charges and increase recombination. These results highlight the importance of using processing additives to balance donor-acceptor interfacial area and domain size to maximize charge separation and minimize recombination, thereby optimizing both J_{sc} and FF .

Conclusions

The effects of DIO on the PBTIBDT:PC₇₁BM solar cell performance are investigated through morphology and exciton dynamics behaviors obtained respectively from X-ray scattering and optical transient absorption. We demonstrate that adding DIO to the active layer solution results in decreased PC₇₁BM aggregate size, but only a slight decrease in donor polymer aggregate size, indicating that DIO selectively dissolves PC₇₁BM and the loosely aggregated PBTIBDT polymer. However, smaller PC₇₁BM aggregates are not observed in either the correlation length or domain size analyses, implying that these small PC₇₁BM aggregates of essentially 1-2 PC₇₁BM molecules do not affect the film crystalline regions and instead modify the amorphous mixed regions. In this particular series of OPV active layer films, we show that DIO primarily affects the degree of mixing between the PBTIBDT polymer and PC₇₁BM molecules. Within the domain size range for the donor polymer and acceptor PC₇₁BM, no significant DIO concentration dependence on the charge separate state decay kinetics is observed on the timescales from sub-ps to many ns. However, a strong DIO concentration dependence on the yield of the polymer cation population is observed over the same timescales, suggesting that increased mixed phase in the PBTIBDT:PC₇₁BM films leads to increased initial cation population, but also enhanced charge recombination. The PBTIBDT:PC₇₁BM solar cells with 3.0

vol% DIO exhibit the best balance between the initial charge generation yield and survival of the charge-separated species, and hence have the highest J_{sc} and FF in this series. From this study it is learned that BHJ morphology can be a bottleneck to optimizing OPV performance and that the best performing devices result from optimal balance between the initial exciton splitting yield and minimization of wasteful charge recombination. Although DIO is only one processing additive among many, this study underscores its importance in the fundamental understanding of additive effects in different steps on OPV function.

Conflict of Interest

There are no conflicts of interest to declare.

Acknowledgement

This research was supported by the ANSER and LEAP Center, an Energy Frontier Research Center funded by the U.S. Department of Energy, Office of Science, Office of Basic Energy Sciences, under Award Number DE-SC0001059. A part of equipment and laboratory setting is supported by the Division of Chemical Sciences, Office of Basic Energy Sciences, the U. S. Department of Energy under contract DE-AC02-06CH11357 (for L. X. C.). The use of the facilities at the Center for Nanoscale Materials was supported by the U. S. Department of Energy, Office of Science, Office of Basic Energy Sciences, under Contract No. DE-AC02-06CH11357. X.G. thanks financial support by the Basic Research fund of Shenzhen City (JCYJ20160530185244662) and Shenzhen Peacock Plan project (KQTD20140630110339343).

References

1. L. Lu, T. Zheng, Q. Wu, A. M. Schneider, D. Zhao and L. Yu, *Chem. Rev.*, 2015, **115**, 12666-12731.
2. M. C. Scharber, *Adv. Mater.*, 2016, **28**, 1994-2001.

3. H. Choi, S.-J. Ko, T. Kim, P.-O. Morin, B. Walker, B. H. Lee, M. Leclerc, J. Y. Kim and A. J. Heeger, *Adv. Mater.*, 2015, **27**, 3318-3324.
4. Y. Lin, F. Zhao, Y. Wu, K. Chen, Y. Xia, G. Li, S. K. K. Prasad, J. Zhu, L. Huo, H. Bin, Z.-G. Zhang, X. Guo, M. Zhang, Y. Sun, F. Gao, Z. Wei, W. Ma, C. Wang, J. Hodgkiss, Z. Bo, O. Inganäs, Y. Li and X. Zhan, *Adv. Mater.*, 2017, **29**, 1604155.
5. C. Q. Yan, S. Barlow, Z. H. Wang, H. Yan, A. K. Y. Jen, S. R. Marder and X. W. Zhan, *Nat. Rev. Mater.*, 2018, **3**, 18003.
6. T. Y. Chu, J. P. Lu, S. Beaupre, Y. G. Zhang, J. R. Pouliot, S. Wakim, J. Y. Zhou, M. Leclerc, Z. Li, J. F. Ding and Y. Tao, *J. Am. Chem. Soc.*, 2011, **133**, 4250-4253.
7. Y. J. Cheng, S. H. Yang and C. S. Hsu, *Chem. Rev.*, 2009, **109**, 5868-5923.
8. M. C. Scharber and N. S. Sariciftci, *Prog. Polym. Sci.*, 2013, **38**, 1929-1940.
9. S. Li, L. Ye, W. Zhao, H. Yan, B. Yang, D. Liu, W. Li, H. Ade and J. Hou, *J. Am. Chem. Soc.*, 2018, **140**, 7159-7167.
10. S. D. Dimitrov and J. R. Durrant, *Chem. Mater.*, 2013, **26**, 616-630.
11. R. Noriega, J. Rivnay, K. Vandewal, F. P. V. Koch, N. Stingelin, P. Smith, M. F. Toney and A. Salleo, *Nature Mater.*, 2013, **12**, 1038-1044.
12. S. A. Hawks, F. Deledalle, J. Yao, D. G. Rebois, G. Li, J. Nelson, Y. Yang, T. Kirchartz and J. R. Durrant, *Adv. Energy Mater.*, 2013, **3**, 1201-1209.
13. J. Kurpiers and D. Neher, *Sci. Rep.*, 2016, **6**, 26832.
14. D. Bartesaghi, I. d. C. Perez, J. Kniepert, S. Roland, M. Turbiez, D. Neher and L. J. A. Koster, *Nat. Commun.*, 2015, **6**, 7083.
15. I. T. Lima, C. Risko, S. G. Aziz, D. A. da Silva and J. L. Bredas, *J. Mater. Chem. C*, 2014, **2**, 8873-8879.
16. K. Zhang, Z. Hu, C. Sun, Z. Wu, F. Huang and Y. Cao, *Chem. Mater.*, 2017, **29**, 141-148.

17. Y. Liu, J. Zhao, Z. Li, C. Mu, W. Ma, H. Hu, K. Jiang, H. Lin, H. Ade and H. Yan, *Nature Commun.*, 2014, **5**, 5293.
18. G. Wang, N. D. Eastham, T. J. Aldrich, B. R. Ma, E. F. Manley, Z. H. Chen, L. X. Chen, M. O. de la Cruz, R. P. H. Chang, F. S. Melkonyan, A. Facchetti and T. J. Marks, *Adv. Energy Mater.*, 2018, **8**, 1702173.
19. A. K. Verma, P. Agnihotri, M. Patel, S. Sahu and S. Tiwari, *Mater. Res. Found.*, 2017, **17**, 299-309.
20. K. Do, M. K. Ravva, T. H. Wang and J. L. Bredas, *Chem. Mater.*, 2017, **29**, 346-354.
21. R. Hildner, A. Kohler, P. Muller-Buschbaum, F. Panzer and M. Thelakkat, *Adv. Energy Mater.*, 2017, **7**, 1700314.
22. Y.-W. Su, S.-C. Lan and K.-H. Wei, 2012, **15**, 554-562.
23. S. M. Ryno, M. K. Ravva, X. K. Chen, H. Y. Li and J. L. Bredas, *Adv. Energy Mater.*, 2017, **7**, 1601370.
24. Y. L. Ma, Z. J. Kang and Q. D. Zheng, *J. Mater. Chem. A*, 2017, **5**, 1860-1872.
25. Y. Zhang, J. Zou, C.-C. Cheuh, H.-L. Yip and A. K. Y. Jen, *Macromolecules*, 2012, **45**, 5427-5435.
26. J.-Y. Wang, S. K. Hau, H.-L. Yip, J. A. Davies, K.-S. Chen, Y. Zhang, Y. Sun and A. K. Y. Jen, *Chem. Mater.*, 2010, **23**, 765-767.
27. R. Stalder, C. Grand, J. Subbiah, F. So and J. R. Reynolds, *Polym. Chem. - UK*, 2012, **3**, 89-92.
28. B. Liu, X. W. Chen, Y. H. He, L. Xiao, Y. F. Li, K. C. Zhou, L. Fan and Y. P. Zou, *RSC Adv.*, 2013, **3**, 5366-5369.
29. W. W. Li, A. Furlan, W. S. C. Roelofs, K. H. Hendriks, G. W. P. van Pruissen, M. M. Wienk and R. A. J. Janssen, *Chem. Commun.*, 2014, **50**, 679-681.

30. B. Pandit, N. E. Jackson, T. Zheng, T. J. Fauvell, E. F. Manley, M. Orr, S. Brown-Xu, L. Yu and L. X. Chen, *J. Phys. Chem. C*, 2016, **120**, 4189-4198.
31. N. E. Jackson, B. M. Savoie, T. J. Marks, L. X. Chen and M. A. Ratner, *J. Phys. Chem. Lett.*, 2015, **6**, 77-84.
32. I. W. Hwang, C. Soci, D. Moses, Z. G. Zhu, D. Waller, R. Gaudiana, C. J. Brabec and A. J. Heeger, *Adv. Mater.*, 2007, **19**, 2307-2312.
33. F. Padinger, R. S. Rittberger and N. S. Sariciftci, *Adv. Funct. Mater.*, 2003, **13**, 85-88.
34. W. J. Grzegorzczak, T. J. Savenije, M. Heeney, S. Tierney, I. McCulloch, S. van Bavel and L. D. A. Siebbeles, *J. Phys. Chem. C*, 2008, **112**, 15973-15979.
35. C. Muller, J. Bergqvist, K. Vandewal, K. Tvingstedt, A. S. Anselmo, R. Magnusson, M. I. Alonso, E. Moons, H. Arwin, M. Campoy-Quiles and O. Inganäs, *J. Mater. Chem.*, 2011, **21**, 10676-10684.
36. J. K. Park, J. Jo, J. H. Seo, J. S. Moon, Y. D. Park, K. Lee, A. J. Heeger and G. C. Bazan, *Adv. Mater.*, 2011, **23**, 2430-2435.
37. N. R. Tummala, C. Sutton, S. G. Aziz, M. F. Toney, C. Risko and J.-L. Bredas, *Chem. Mater.*, 2015, **27**, 8261-8272.
38. Z. F. Li, Q. F. Dong, S. Y. Yao, J. Y. Qian, Y. L. Wang, F. Y. Jiang, H. Yang, Q. Zhao, Q. F. Hou, W. Meng, J. H. Tong, S. X. Xiong and W. J. Tian, *J. Mater. Sci.*, 2015, **50**, 937-947.
39. Z. He, C. Zhong, S. Su, M. Xu, H. Wu and Y. Cao, *Nat. Photonics*, 2012, **6**, 591-595.
40. T. J. Aldrich, S. M. Swick, F. S. Melkonyan and T. J. Marks, *Chem. Mater.*, 2017, **29**, 10294-10298.
41. S. Wakim, S. Beaupre, N. Blouin, B. R. Aich, S. Rodman, R. Gaudiana, Y. Tao and M. Leclerc, *J. Mater. Chem.*, 2009, **19**, 5351-5358.

42. H. Hoppe, M. Niggemann, C. Winder, J. Kraut, R. Hiesgen, A. Hinsch, D. Meissner and N. S. Sariciftci, *Adv. Funct. Mater.*, 2004, **14**, 1005-1011.
43. S. H. Park, A. Roy, S. Beaupre, S. Cho, N. Coates, J. S. Moon, D. Moses, M. Leclerc, K. Lee and A. J. Heeger, *Nature Photon.*, 2009, **3**, 297-303.
44. C. Muller, T. A. M. Ferenczi, M. Campoy-Quiles, J. M. Frost, D. D. C. Bradley, P. Smith, N. Stingelin-Stutzmann and J. Nelson, *Adv. Mater.*, 2008, **20**, 3510-3515.
45. L. Huo, T. Liu, X. Sun, Y. Cai, A. J. Heeger and Y. Sun, *Adv. Mater.*, 2015, **27**, 2938-2944.
46. C. Liu, C. Yi, K. Wang, Y. Yang, R. S. Bhatta, M. Tsige, S. Xiao and X. Gong, *Acs Appl. Mater. Inter.*, 2015, **7**, 4928-4935.
47. J. S. Moon, C. J. Takacs, S. Cho, R. C. Coffin, H. Kim, G. C. Bazan and A. J. Heeger, *Nano Lett.*, 2010, **10**, 4005-4008.
48. B. R. Aich, J. P. Lu, S. Beaupre, M. Leclerc and Y. Tao, *Org. Electron.*, 2012, **13**, 1736-1741.
49. F. C. Chen, H. C. Tseng and C. J. Ko, *Appl. Phys. Lett.*, 2008, **92**, 103316.
50. C. V. Hoven, X. D. Dang, R. C. Coffin, J. Peet, T. Q. Nguyen and G. C. Bazan, *Adv. Mater.*, 2010, **22**, E63-E66.
51. J. K. Lee, W. L. Ma, C. J. Brabec, J. Yuen, J. S. Moon, J. Y. Kim, K. Lee, G. C. Bazan and A. J. Heeger, *J. Am. Chem. Soc.*, 2008, **130**, 3619-3623.
52. H.-J. Jhuo, S.-H. Liao, Y.-L. Li, P.-N. Yeh, S.-A. Chen, W.-R. Wu, C.-J. Su, J.-J. Lee, N. L. Yamada and U. S. Jeng, *Adv. Funct. Mater.*, 2016, **26**, 3094-3104.
53. J. Zhao, Y. Li, G. Yang, K. Jiang, H. Lin, H. Ade, W. Ma and H. Yan, *Nature Energ.*, 2016, **1**, 15027.
54. K. R. Graham, P. M. Wieruszewski, R. Stalder, M. J. Hartel, J. G. Mei, F. So and J. R. Reynolds, *Adv. Funct. Mater.*, 2012, **22**, 4801-4813.

55. D. T. Duong, B. Walker, J. Lin, C. Kim, J. Love, B. Purushothaman, J. E. Anthony and T. Q. Nguyen, *J. Polym. Sci. Pol. Phys.*, 2012, **50**, 1405-1413.
56. J. Kniepert, I. Lange, J. Heidbrink, J. Kurpiers, T. J. K. Brenner, L. J. A. Koster and D. Neher, *J. Phys. Chem. C*, 2015, **119**, 8310-8320.
57. F. S. U. Fischer, D. Trefz, J. Back, N. Kayunkid, B. Tornow, S. Albrecht, K. G. Yager, G. Singh, A. Karim, D. Neher, M. Brinkmann and S. Ludwigs, *Adv. Mater.*, 2015, **27**, 1223-1228.
58. J. Peet, N. S. Cho, S. K. Lee and G. C. Bazan, *Macromolecules*, 2008, **41**, 8655-8659.
59. M. T. Dang and J. D. Wuest, *Chem. Soc. Rev.*, 2013, **42**, 9105-9126.
60. J. T. Rogers, K. Schmidt, M. F. Toney, G. C. Bazan and E. J. Kramer, *J. Am. Chem. Soc.*, 2012, **134**, 2884-2887.
61. T. H. Lee, S. Y. Park, B. Walker, S.-J. Ko, J. Heo, H. Y. Woo, H. Choi and J. Y. Kim, *Rsc Adv.*, 2017, **7**, 7476-7482.
62. E. F. Manley, J. Strzalka, T. J. Fauvell, N. E. Jackson, M. J. Leonardi, N. D. Eastham, T. J. Marks and L. X. Chen, *Adv. Mater.*, 2017, **29**, 1703933.
63. E. F. Manley, J. Strzalka, T. J. Fauvell, T. J. Marks and L. X. Chen, *Adv. Energy Mater.*, 2018, DOI: doi:10.1002/aenm.201800611, 1800611.
64. Y. Liang, Z. Xu, J. B. Xia, S. T. Tsai, Y. Wu, G. Li, C. Ray and L. P. Yu, *Adv. Mater.*, 2010, **22**, E135-E138.
65. B. A. Collins, Z. Li, J. R. Tumbleston, E. Gann, C. R. McNeill and H. Ade, *Adv. Energy Mater.*, 2013, **3**, 65-74.
66. N. Shin, L. J. Richter, A. A. Herzing, R. J. Kline and D. M. DeLongchamp, *Adv. Energy Mater.*, 2013, **3**, 938-948.

67. Z. H. Mao, T. P. Le, K. Vakhshouri, R. Fernando, F. Ruan, E. Muller, E. D. Gomez and G. Sauve, *Org. Electron.*, 2014, **15**, 3384-3391.
68. X. Zhang, C. L. Zhan and J. N. Yao, *Chem. Mater.*, 2015, **27**, 166-173.
69. W. Huang, E. Gann, L. Thomsen, C. Dong, Y.-B. Cheng and C. R. McNeill, *Adv. Energy Mater.*, 2015, **5**, 1401259.
70. C. J. Schaffer, J. Schlipf, E. D. Indari, B. Su, S. Bernstorff and P. Muller-Buschbaum, *Acs Appl. Mater. Inter.*, 2015, **7**, 21347-21355.
71. M.-S. Su, C.-Y. Kuo, M.-C. Yuan, U.-S. Jeng, C.-J. Su and K.-H. Wei, 2011, **23**, 3315-3319.
72. C.-M. Liu, Y.-W. Su, J.-M. Jiang, H.-C. Chen, S.-W. Lin, C.-J. Su, U. S. Jeng and K.-H. Wei, 2014, **2**, 20760-20769.
73. F. Gao, S. Himmelberger, M. Andersson, D. Hanifi, Y. X. Xia, S. Q. Zhang, J. P. Wang, J. H. Hou, A. Salleo and O. Inganäs, *Adv. Mater.*, 2015, **27**, 3868.
74. S. Sweetnam, R. Prasanna, T. M. Burke, J. A. Bartelt and M. D. McGehee, *J. Phys. Chem. C*, 2016, **120**, 6427-6434.
75. C. H. Woo, P. M. Beaujuge, T. W. Holcombe, O. P. Lee and J. M. J. Fréchet, *J. Am. Chem. Soc.*, 2010, **132**, 15547-15549.
76. Y.-W. Su, C.-M. Liu, J.-M. Jiang, C.-S. Tsao, H.-C. Cha, U. S. Jeng, H.-L. Chen and K.-H. Wei, 2015, **119**, 3408-3417.
77. S. Guo, W. Wang, E. M. Herzig, A. Naumann, G. Tainter, J. Perlich and P. Müller-Buschbaum, *Acs Appl. Mater. Inter.*, 2017, **9**, 3740-3748.
78. S. J. Lou, J. M. Szarko, T. Xu, L. P. Yu, T. J. Marks and L. X. Chen, *J. Am. Chem. Soc.*, 2011, **133**, 20661-20663.
79. S. Mukherjee, X. Jiao and H. Ade, *Adv. Energy Mater.*, 2016, **6**, 1600699.

80. S. Mukherjee, C. M. Proctor, G. C. Bazan, T. Q. Nguyen and H. Ade, *Adv. Energy Mater.*, 2015, **5**, 1500877.
81. S. Sweetnam, K. R. Graham, G. O. Ngongang Ndjawa, T. Heumüller, J. A. Bartelt, T. M. Burke, W. Li, W. You, A. Amassian and M. D. McGehee, *J. Am. Chem. Soc.*, 2014, **136**, 14078-14088.
82. N. D. Eastham, A. S. Dudnik, T. J. Aldrich, E. F. Manley, T. J. Fauvell, P. E. Hartnett, M. R. Wasielewski, L. X. Chen, F. S. Melkonyan, A. Facchetti, R. P. H. Chang and T. J. Marks, *Chem. Mater.*, 2017, **29**, 4432-4444.
83. X. G. Guo, N. J. Zhou, S. J. Lou, J. Smith, D. B. Tice, J. W. Hennek, R. P. Ortiz, J. T. L. Navarrete, S. Y. Li, J. Strzalka, L. X. Chen, R. P. H. Chang, A. Facchetti and T. J. Marks, *Nat. Photonics*, 2013, **7**, 825-833.
84. W. L. Rance, A. J. Ferguson, T. McCarthy-Ward, M. Heeney, D. S. Ginley, D. C. Olson, G. Rumbles and N. Kopidakis, *Acs Nano*, 2011, **5**, 5635-5646.
85. S. Few, J. M. Frost, J. Kirkpatrick and J. Nelson, *J. Phys. Chem. C*, 2014, **118**, 8253-8261.
86. A. A. Y. Guilbert, M. Schmidt, A. Bruno, J. Yao, S. King, S. M. Tuladhar, T. Kirchartz, M. I. Alonso, A. R. Goñi, N. Stingelin, S. A. Haque, M. Campoy-Quiles and J. Nelson, *Adv. Funct. Mater.*, 2014, **24**, 6972-6980.
87. S. J. Oh, J. Kim, J. M. Mativetsky, Y.-L. Loo and C. R. Kagan, *Acs Appl. Mater. Inter.*, 2016, **8**, 28743-28749.
88. B. A. Collins, E. Gann, L. Guignard, X. He, C. R. McNeill and H. Ade, *J. Phys. Chem. Lett.*, 2010, **1**, 3160-3166.
89. J. B. You, C. C. Chen, Z. R. Hong, K. Yoshimura, K. Ohya, R. Xu, S. L. Ye, J. Gao, G. Li and Y. Yang, *Adv. Mater.*, 2013, **25**, 3973-3978.

90. H. Xin, X. G. Guo, G. Q. Ren, M. D. Watson and S. A. Jenekhe, *Adv. Energy Mater.*, 2012, **2**, 575-582.
91. B. A. Collins, Z. Li, J. R. Tumbleston, E. Gann, C. R. McNeill and H. Ade, *Adv. Energy Mater.*, 2012, **3**, 65-74.
92. C. Zhou, G. Zhang, C. Zhong, X. Jia, P. Luo, R. Xu, K. Gao, X. Jiang, F. Liu, T. P. Russell, F. Huang and Y. Cao, *Adv. Energy Mater.*, 2017, **7**, 1601081.
93. J. Yuan, M. Ford, W. Ma and G. C. Bazan, *J. Mater. Chem. A*, 2017, **5**, 8903-8908.
94. M. Scarongella, J. De Jonghe-Risse, E. Buchaca-Domingo, M. Causa, Z. P. Fei, M. Heeney, J. E. Moser, N. Stingelin and N. Banerji, *J. Am. Chem. Soc.*, 2015, **137**, 2908-2918.
95. L. G. Kaake, G. C. Welch, D. Moses, G. C. Bazan and A. J. Heeger, *J. Phys. Chem. Lett.*, 2012, **3**, 1253-1257.
96. S. Huettner, J. M. Hodgkiss, M. Sommer, R. H. Friend, U. Steiner and M. Thelakkat, *J. Phys. Chem. B*, 2012, **116**, 10070-10078.
97. C. Poelking and D. Andrienko, *J. Am. Chem. Soc.*, 2015, **137**, 6320-6326.
98. M. C. Scharber, C. Lungenschmied, H. J. Egelhaaf, G. Matt, M. Bednorz, T. Fromherz, J. Gao, D. Jarzab and M. A. Loi, *Energ. Environ. Sci.*, 2011, **4**, 5077-5083.
99. A. C. Jakowetz, M. L. Böhm, J. Zhang, A. Sadhanala, S. Huettner, A. A. Bakulin, A. Rao and R. H. Friend, *J. Am. Chem. Soc.*, 2016, **138**, 11672-11679.
100. G. Grancini, N. Martino, M. R. Antognazza, M. Celebrano, H.-J. Egelhaaf and G. Lanzani, *J. Phys. Chem. C*, 2012, **116**, 9838-9844.
101. N. D. Eastham, J. L. Logsdon, E. F. Manley, T. J. Aldrich, M. J. Leonardi, G. Wang, N. E. Powers-Riggs, R. M. Young, L. X. Chen, M. R. Wasielewski, F. S. Melkonyan, R. P. H. Chang and T. J. Marks, *Adv Mater*, 2018, **30**, 1704263.

102. N. J. Zhou, X. G. Guo, R. P. Ortiz, S. Q. Li, S. M. Zhang, R. P. H. Chang, A. Facchetti and T. J. Marks, *Adv. Mater.*, 2012, **24**, 2242-2248.
103. H. Huang, L. Yang, A. Facchetti and T. J. Marks, *Chem. Rev.*, 2017, **117**, 10291-10318.
104. K. Vandewal, K. Tvingstedt, A. Gadisa, O. Inganäs and J. V. Manca, 2009, **8**, 904.
105. J. Ilavsky and P. R. Jemian, *J. Appl. Crystallogr.*, 2009, **42**, 347-353.
106. G. Beaucage, *J. Appl. Crystallogr.*, 1996, **29**, 134-146.
107. G. Beaucage, *J. Appl. Crystallogr.*, 1995, **28**, 717-728.
108. B. Hammouda, *J. Appl. Crystallogr.*, 2010, **43**, 716-719.
109. D. M. Smilgies, *J. Appl. Crystallogr.*, 2009, **42**, 1030-1034.
110. A. A. Bakulin, S. D. Dimitrov, A. Rao, P. C. Y. Chow, C. B. Nielsen, B. C. Schroeder, I. McCulloch, H. J. Bakker, J. R. Durrant and R. H. Friend, *J. Phys. Chem. Lett.*, 2013, **4**, 209-215.
111. R. Andernach, H. Utzat, S. D. Dimitrov, I. McCulloch, M. Heeney, J. R. Durrant and H. Bronstein, *J. Am. Chem. Soc.*, 2015, **137**, 10383-10390.
112. E. Collado-Fregoso, P. Boufflet, Z. Fei, E. Gann, S. Ashraf, Z. Li, C. R. McNeill, J. R. Durrant and M. Heeney, *Chem. Mater.*, 2015, **27**, 7934-7944.
113. T. J. Fauvell, T. Y. Zheng, N. E. Jackson, M. A. Ratner, L. P. Yu and L. X. Chen, *Chem. Mater.*, 2016, **28**, 2814-2822.
114. B. S. Rolczynski, J. M. Szarko, H. J. Son, L. P. Yu and L. X. Chen, *J. Phys. Chem. Lett.*, 2014, **5**, 1856-1863.
115. Y. W. Soon, S. Shoaee, R. S. Ashraf, H. Bronstein, B. C. Schroeder, W. Zhang, Z. Fei, M. Heeney, I. McCulloch and J. R. Durrant, *Adv. Funct. Mater.*, 2014, **24**, 1474-1482.
116. K. J. Li, P. P. Khlyabich, L. J. Li, B. Burkhart, B. C. Thompson and J. C. Campbell, *J. Phys. Chem. C*, 2013, **117**, 6940-6948.

117. G. F. A. Dibb, F. C. Jamieson, A. Maurano, J. Nelson and J. R. Durrant, *J. Phys. Chem. Lett.*, 2013, **4**, 803-808.
118. M. H. Jao, H. C. Liao and W. F. Su, *J. Mater. Chem. A*, 2016, **4**, 5784-5801.
119. J. C. Guo, Y. Y. Liang, J. Szarko, B. Lee, H. J. Son, B. S. Rolczynski, L. P. Yu and L. X. Chen, *J. Phys. Chem. B*, 2010, **114**, 742-748.
120. I. A. Howard, R. Mauer, M. Meister and F. Laquai, *J. Am. Chem. Soc.*, 2010, **132**, 14866-14876.

